






Non-contact imaging of terahertz surface currents with aperture-type near-field microscopy

SARAH NORMAN,^{1,*} JAMES SEDDON,¹  YUEZHEN LU,¹ LUCY HALE,²  ABDULLAH ZAMAN,³ SADHVIKAS J. ADDAMANE,^{4,5} IGAL BRENER,^{4,5} RICCARDO DEGL'INNOCENTI,⁶  AND OLEG MITROFANOV^{1,4}

¹University College London, Electronic and Electrical Engineering, London WC1E 7JE, UK

²ETH Zurich, Institute of Quantum Electronics, Auguste-Piccard-Hof 1, 8093 Zurich, Switzerland

³Lancaster University, School of Engineering, New Engineering Building, Gillow Ave, Bailrigg, Lancaster LA1 4YW, UK

⁴Center for Integrated Nanotechnologies, Sandia National Laboratories, Albuquerque, New Mexico 87123, USA

⁵Sandia National Laboratories, Albuquerque, New Mexico 87123, USA

⁶Queen Mary University of London, School of Electronic Engineering and Computer Science, London E1 4NS, UK

*sarah.norman.21@ucl.ac.uk

Abstract: Terahertz (THz) near-field imaging and spectroscopy provide valuable insights into the fundamental physical processes occurring in THz resonators and metasurfaces on the subwavelength scale. However, so far, the mapping of THz surface currents has remained outside the scope of THz near-field techniques. In this study, we demonstrate that aperture-type scanning near-field microscopy enables non-contact imaging of THz surface currents in subwavelength resonators. Through extensive near-field mapping of an asymmetric D-split-ring THz resonator and full electromagnetic simulations of the resonator and the probe, we demonstrate the correlation between the measured near-field images and the THz surface currents. The observed current dynamics in the interval of several picoseconds reveal the interplay between several excited modes, including dark modes, whereas broadband THz near-field spectroscopy analysis enables the characterization of electromagnetic resonances defined by the resonator geometry.

Published by Optica Publishing Group under the terms of the [Creative Commons Attribution 4.0 License](https://creativecommons.org/licenses/by/4.0/). Further distribution of this work must maintain attribution to the author(s) and the published article's title, journal citation, and DOI.

1. Introduction

Metamaterials and metasurfaces have introduced a versatile platform to control light and engineer light-matter interactions by employing arrays of subwavelength scale resonators [1–3]. Metasurfaces with advanced designs now exploit polarization-sensitive multiple photonic states to achieve desired functionalities [4–10]. Concurrently, near-field spectroscopy and imaging techniques have provided a valuable tool for their characterization [11–34]. In contrast to far-field techniques, near-field approaches enable direct excitation and sampling of evanescent fields in individual resonators [13–16,35]. In the terahertz (THz) frequency range in particular, near-field techniques have revealed excitations and field distributions in THz resonators of various designs and made of different materials [11,13,15,18,23,35,36] including topological insulators [28,29]. While near-field methods provide access to the scientifically rich domain of subwavelength-scale electromagnetics, they still suffer from the complexity of elaborate experimental configurations and signal processing techniques, which leads to the central question of near-field signal

interpretation [11,13,15,18,23,37,38]. Various THz near-field imaging configurations have revealed a multitude of physical phenomena, including the accumulation of charge carriers at the nanoscale [30], launching of THz surface plasmon waves [18,21,22,28,29,31–33] and detection of vectorial components of THz resonant fields [34]. However, near-field mapping of THz surface currents so far has remained beyond the scope of near-field techniques, despite the key role these currents play in determining the response of resonators and metasurfaces [39–41].

Here, we demonstrate the potential of aperture-type THz near-field imaging and spectroscopy to detect surface currents in an individual asymmetric D-split-ring resonator and map their spatial distribution evolving on the picosecond time scale. This resonator design supports several polarization-sensitive modes, featuring distinctive surface current patterns [4,5,42,43]. By using two orthogonal incident THz beam polarizations in our experiments and employing rigorous electromagnetic simulations of the resonator and the full near-field probe, we demonstrate that the spatial maps recorded by an aperture-type THz near-field probe with an integrated detector [44] enable accurate reconstruction of the resonator's surface current distributions on the subwavelength scale. Interestingly, in both, simulated and experimental spatial maps, we observe a higher spatial resolution than that expected from the probe aperture size [45]. The ability to reveal THz surface current distributions and their dynamics on the picosecond time scale with subwavelength spatial resolution and broadband THz spectroscopy analysis can open doors to detailed mode characterization in plasmonic THz metamaterials and resonators.

2. Results and discussion

2.1. THz near-field measurements

Figure 1(a) illustrates the asymmetric D-split-ring resonator (ADSR) design featuring two metallic D-shaped ring halves with asymmetric gaps and two connecting bars in the center. This design was first investigated as THz resonator arrays using far-field THz spectroscopy [42], and more recently as single resonators using aperture-type THz near-field spectroscopy [43]. Here, we adopted the resonator design and fabricated resonators to support several modes in the range of 0.7–2.5 THz with relatively high Q-factors enabled by a low-loss quartz substrate. Details of the design and the fabrication process are reported in [Supplement 1](#).

A single resonator was illuminated at normal incidence from the substrate side with short THz pulses generated by an InAs source in a standard THz time-domain spectroscopy setup pumped by 100 femtosecond pulsed light from a Ti:Sapphire laser [46]. THz near-field maps were recorded in the time domain using an aperture-type THz near-field probe (Fig. 1(b)). The probe featuring a gold planar surface with a $10 \times 10 \mu\text{m}^2$ aperture and an integrated photoconductive antenna THz detector was positioned at $\sim 5 \pm 2 \mu\text{m}$ from the sample.

The near-field probe directly detects evanescent THz fields coupled through the aperture and it is sensitive to two electric field quantities: (1) the temporal derivative of the electric field component parallel to the antenna orientation (along the x -axis), $\frac{dE_x}{dt}$; and (2) the spatial derivative of the out-of-plane field component $\frac{dE_z}{dx}$. The second quantity tends to dominate the near-field signal when the near-field probe is positioned over metallic regions [22,31,46]. By raster scanning the resonator over the probe at selected points in time during the excitation by the short THz pulse, we can map a combination of these two quantities in the xy -plane.

2.2. Single-mode regime

In the first experiment, we focused on a resonator excited with THz pulses polarized along the x -axis, parallel to the resonator's central bars (co-polarized). This configuration allowed excitation of the dominant dipolar mode at ~ 0.76 THz. To gain insight into this process, we modeled the resonator response and its surface current distributions using finite integration technique (FIT) full-wave simulations in CST Microwave Solver. Following the excitation,

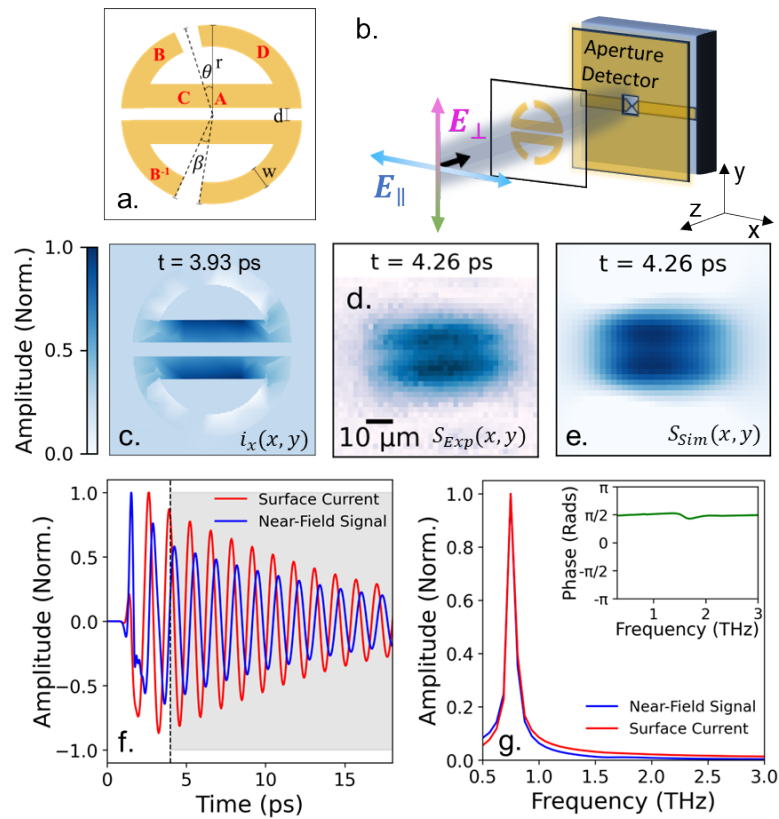


Fig. 1. (a) Layout of the ADSR resonator illustrating key resonator parameters and labeled A-D probe positions of near-field measurements. (b) Schematic of the near-field setup. (c)-(e) Comparison of simulated surface current distribution (c) with measured (d) and simulated (e) near-field spatial maps obtained with the aperture probe. The measurement was conducted with a co-polarized incident electric field, at a moment of maximum near-field signal during one of the oscillations in the time-domain waveform. (f) *Blue line*: simulated time-domain waveform of the near-field signal at location A; *red line*: simulated dynamics of the surface current at the same location. (g) Corresponding Fourier amplitude spectra and their phase difference (inset) showing a $\pi/2$ phase shift.

oscillating surface currents develop in the resonator. The current distribution in the two halves has equal x-components oscillating in phase and equal y-components oscillating in antiphase. The x-component distribution of the current shows two regions of maximum current along the central bars corresponding to parallel currents circulating in phase in the top and bottom halves of the resonator (Fig. 1(c)). The currents oscillate at the frequency of 0.76 THz and the oscillations persist for several cycles (Fig. 1(f),(g)).

In the experiment, we recorded a near-field THz map after the short THz pulse excitation ($t = 4.26$ ps), $S_{Exp}(x,y)$, which closely resembles the simulated dipole-like surface current distribution, with two regions of stronger near-field signal along the central bars of the resonator (Fig. 1(d)). The aperture-type probe was previously found to detect the spatial derivative of the E_z field component of surface plasmon waves [31], $\frac{dE_z}{dx}$. However, this quantity is directly linked to the surface currents in the resonator: a current along the x -axis $i_x(x,y)$ redistributes charges on the resonator surface and these charges create an electric field normal to the surface, E_z , which varies along the x -axis. The aperture-type near-field probe therefore has the potential to reveal the distribution of surface currents.

To test this hypothesis, we developed a full numerical simulation of the entire near-field probe (including the THz detector antenna) and the resonator. The simulations of the THz antenna behind the $10 \times 10 \mu\text{m}^2$ aperture allowed us to numerically model the near-field signal, as it is proportional to the voltage induced between the detector antenna tips. We then simulated the raster-scanning of the resonator over the aperture, recording the voltage between the tips for every position of the resonator. Combining the data from each resonator position allowed us to construct very accurate spatial maps of the near-field signal, $S_{Sim}(x,y)$, for every moment in time. A simulated map showed excellent agreement with the experimental map (Fig. 1(d) and 1(e)), confirming that the near-field maps collected with the aperture probe indeed reveal the distribution of surface currents in the resonator.

The simulations, with the ability to reproduce the near-field signal and its accuracy, also provide a method for correlating the time-domain near-field signal to the surface current temporal evolution. In Fig. 1(f), we compare time-domain waveforms of the simulated near-field signal at the top central bar and the surface current at the same location (A). Both waveforms show harmonic oscillations after the THz pulse excitation. Fourier transforms of the two waveforms confirm that the oscillations are characterized by the same frequency and the same resonance linewidth (Fig. 1(g)). We obtained practically identical amplitude spectra for the simulated surface current and the near-field probe signal. We also observed a constant $\pi/2$ phase shift between the surface current and the detected signal. The phase shift can be understood after considering the nature of the detected near-field signal: the surface current leads to charge redistribution within the resonator, creating an imbalance of charge and the corresponding normal electric field. This field is detected by the near-field probe. Since the total charge (and the field) is proportional to the time integral of the current, the detected near-field signal lags the current dynamics. In the case of the surface current oscillating in resonance (Fig. 1(f)), the detected signal results in the $\pi/2$ phase shift. The inset of Fig. 1(g) shows the phase shift spectrum obtained by comparing the Fourier spectra of the surface current and near-field signal within the gray area in Fig. 1(f), which excludes the transient period of resonator excitation (0-4 ps). The phase shift spectrum obtained using the entire waveforms is shown in [Supplement 1](#).

These results demonstrate that experimental near-field maps accurately reconstruct the distribution of surface currents in the resonator and the time-domain spectroscopy analysis precisely provides the corresponding resonance properties in the single-mode regime. In the following section, we verify whether these findings hold in more complex cases of multimode resonator excitation. In these cases, experimental near-field observations can offer insights into the dynamic interplay between the resonator's current distributions associated with specific resonator modes. We will use the comprehensive model of the near-field probe in the numerical simulations to

precisely verify the expected near-field spatial maps and their dynamics not only following the short THz pulse excitation, but also during the excitation.

2.3. Multimode regime

We now examine the correlation between the experimental near-field maps and the surface current maps when several resonances are excited simultaneously. We considered the same resonator but changed the polarization of the incident THz field. The orthogonally polarized pulse (with the electric field perpendicular to the resonator central bars, or cross-polarized) excites several modes including a “dark” mode [43]. These modes are excellent for testing the ability of the near-field probe to map the surface current distribution, as they are described by their distinctive current distribution patterns [4,5,42,43]. In particular, the dark mode exhibits an antisymmetric current pattern in the upper and lower halves of the resonator [42]. We note that in the cross-polarized illumination experiment, the near-field probe is blind to the incident pulse field, and it only detects the resonator-induced signal along the x-axis.

Figure 2(a) displays experimental near-field maps of the resonator measured at two selected times, 1.69 ps and 2.36 ps. Numerical simulations of the experiment (Fig. 2(a), bottom panel) closely resembles the experimental maps. Notably, both the experimental and simulated maps show a higher spatial resolution than expected from the aperture size (10 μm) [45], revealing small features such as the gap in the arch of the resonator, which measures approximately 6 μm .

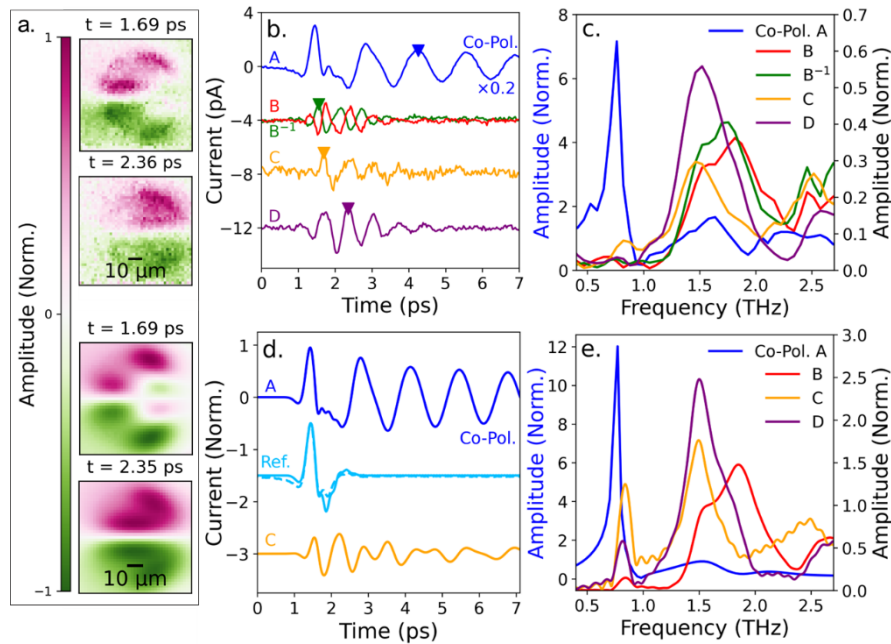


Fig. 2. (a) Measured and simulated near-field signal maps for cross-polarized incident electric field configuration; the maps were measured at $t = 1.69$ and 2.36 ps. (b) Time-domain near-field signal measured in positions A–D, with triangles indicating the time instances when the spatial maps in (a) were produced (yellow and purple triangles). (c) Measured spectral amplitude normalized to the reference spectrum acquired at a substrate-only area of the sample (dashed blue waveform in panel (d)). (d) Simulated near-field signal for the near-field probe at positions A and C, compared to the incident pulse waveforms (Reference): simulated (solid) and measured (dashed). (e) Simulated spectral amplitude in positions A – D normalized to the simulated reference spectrum.

High THz signal areas in the maps indicate locations where the resonator modes exhibit peak amplitudes in the near-field signal. To analyze these modes, in Fig. 2(b) we show the near-field signal waveforms recorded at selected locations (marked as B, B⁻¹, C and D in Fig. 1(a)), and the corresponding Fourier spectra in Fig. 2(c). The spectra were normalized to a reference spectrum (measured in the co-polarized configuration, blue solid and dashed waveforms in Fig. 2(d)). The normalized near-field signal spectra show four modes with different peak amplitudes at different locations on the resonator (Fig. 2(b) and (c)). These peaks correspond to the dark mode at ~0.84 THz and higher order modes at ~1.50, ~1.82 and ~2.50 THz, consistent with previous near-field cross-polarized measurements on similar resonators [43]. The experimental spectra align well with the simulated spectra, as illustrated in Fig. 2(e), although we observed a diminished dark mode peak (see Supplement 1 for further details).

The Fourier analysis shows that multiple modes are simultaneously excited in the resonator. Therefore, comparing the surface current distribution to the near-field spatial maps recorded in time-domain becomes more complex. As the excited modes superimpose, the corresponding surface current distribution is now a superposition varying in time. Furthermore, the $\pi/2$ phase shift for every mode now corresponds to a different moment in time. To mitigate this difficulty, we can compare surface current distributions and measured spatial maps at moments in time, when surface current oscillations at a single frequency dominate. This can occur under two conditions. Firstly, when only one mode remains in the tail of the waveform, and in this resonator design, the dark mode remains in the resonator the longest, while the other modes have already decayed (see Supplement 1, Fig. 3). This regime is similar to the single-mode excitation which we have already discussed. Secondly, at the signal's onset when the resonator responds to the incident THz pulse, surface currents in the resonator are 'driven' at the central frequency of the incident THz pulse. In this second case, the $\pi/2$ phase shift is well defined in time. It corresponds to $t = T_d/4$, where $T_d = 1.01$ ps is the inverse of the pulse's central frequency.

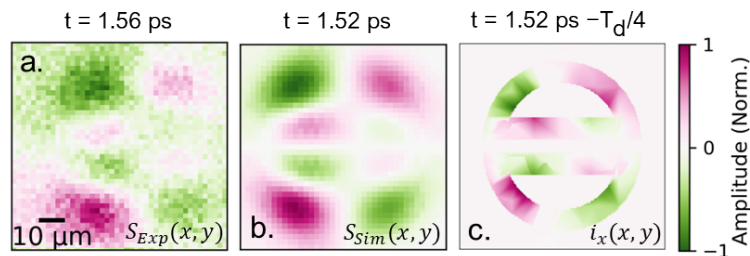


Fig. 3. (a) Measured and (b) simulated near-field spatial maps measured at the signal onset where the resonator is driven by the field of the incident THz pulse ($t = 1.52$ ps). (c) Corresponding simulated surface current distribution at $t = 1.52 - T_d/4$, where $T_d/4$, represents a $\pi/2$ phase shift at the pulse's central frequency, $1/T_d$.

Figure 3(a) and (b) show an experimental near-field map at the pulse's onset and the corresponding simulated image. Using the $\pi/2$ phase shift for the driving frequency, we can find the related surface current distribution (shown in Fig. 3(c)). The near-field signal distribution, which corresponds to the x-component of the current, reveals alternating regions of positive (+1) and negative (-1) currents in the central bars and curved arms of the resonator. The pattern resembles a standing wave pattern of a high order mode, where the current direction alternates along the upper and lower resonator rings. One can observe a clear positive signal at position B⁻¹, with a mirrored negative signal on the opposite half of the resonator (position B). The same patterns can be seen in the simulated surface current distribution (c) and in the simulated near-field image (b). There is excellent agreement between the three maps, highlighting that even in the complex case of multimode excitation, near-field images recorded by the aperture-type

probe can represent the current distribution in the resonator. This technique can therefore serve as an effective tool to investigate not only single-mode excitation, as shown in Fig. 1, but also multimode surface current excitations, as depicted in Fig. 2.

As a final comment, we note that maps of surface currents in the resonator can be also obtained in the frequency domain. It would enable direct correlation of experimental near-field maps to the current distributions for individual modes. This analysis however requires lengthy acquisition of full THz time-domain waveforms for every point in the map, and it is beyond the scope of this work. Nevertheless, we can use our numerical model of the near-field signal to compare simulated near-field images with the current distributions at the frequencies of individual modes. These maps are compared in Fig. 4 for the supported modes when excited by co-polarized (Fig. 4(a) and (d)) and cross-polarized (Fig. 4(b,c,e,f)) THz pulses: the bright mode at ~ 0.76 THz, the dark mode at ~ 0.84 THz and the mode at ~ 1.50 THz.

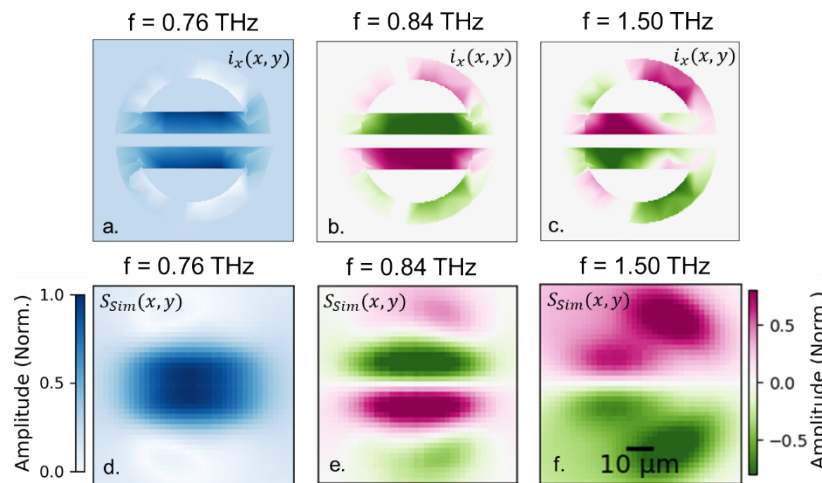


Fig. 4. (a)-(c) Simulated current distributions and (d)-(f) near-field spatial maps at three resonances excited with co-polarized (a),(d) and cross-polarized (b),(c),(e),(f) incident electric field. The color scale for the modes excited by cross-polarized THz pulses is condensed to enhance the color saturation and show the distribution across the entire resonator.

Once again, we observe a strong resemblance between the simulated near-field probe maps and the surface current distributions. Notably, the frequency-domain spatial maps (and the corresponding current distributions) in Figs. 4(d) and (f) closely mirror the time-domain maps in Fig. 1(d) and Fig. 2(a), respectively. In the latter case, it suggests that the dominant mode in the resonator at that moment ($t \sim 1.69$ ps, Fig. 2) is the 1.50 THz mode, even though it decays rapidly. The local near-field spectra (Fig. 2) confirm that the 1.50 THz mode is the dominant mode (based on the mode's relative amplitude). It is important to note that in all the figures, the simulated current distributions only depict the x -component of the surface current for direct comparison to the experimental results. The orthogonal component of the surface current can be mapped by rotating the near-field probe by 90 degrees.

3. Conclusion

This work highlights the unique potential of aperture-type THz near-field microscopy for investigations of surface currents and their dynamics in individual conductive THz resonators. We have demonstrated that experimental near-field maps enable accurate reconstruction of the surface currents distribution and its evolution in the asymmetric D-split-ring resonator for

single-mode and multimode excitation cases. The local time-domain spectroscopy analysis is particularly powerful in the latter cases, as it enables extracting the resonance properties and the corresponding spatial distribution of surface currents. We supported our analysis with full numerical simulations of the near-field signal recorded by the aperture-type near-field probe. The simulations also allowed us to confirm that the experimental near-field measurements with the aperture-type probe tend to exhibit a spatial resolution better than the expected spatial resolution based on the aperture size. We anticipate that the unique capability to map THz surface currents in subwavelength-size THz resonators demonstrated in this work, will facilitate the research on plasmonic THz metamaterials and metasurfaces by providing useful insights into the physics of devices made from conventional and emerging materials, including superconductors and topological insulators [39–41,47]. While the aperture-type near-field probe is limited in spatial resolution, the resolution is sufficient for mapping the patterns of surface currents in THz resonators with features as small $\sim 5 \mu\text{m}$.

Acknowledgments. This work was supported by the Engineering and Physical Sciences Research Council (EP/S022139/1) - the Centre for Doctoral Training in Connected Electronic and Photonic Systems, EP/W028921/1 – TERACOM, EPSRC (Grant No. EP/S019383/1), (Grant No. EP/T517793/1), Chinese Scholarship Council (CSC-202108890030), and the U.S. Department of Energy (DOE), Office of Basic Energy Sciences, Division of Materials Sciences and Engineering. This work was performed, in part, at the Center for Integrated Nanotechnologies, an Office of Science User Facility operated for the U.S. DOE Office of Science. SNL is managed and operated by NTESS under DOE NNSA contract DE-NA0003525.

Disclosures. The authors declare no conflicts of interest.

Data availability. The data underlying the results presented in this paper are not publicly available at this time but may be obtained from the authors upon reasonable request.

Supplemental document. See [Supplement 1](#) for supporting content.

References

1. H.-T. Chen, A. J. Taylor, and N. Yu, “A review of metasurfaces: physics and applications,” *Rep. Prog. Phys.* **79**(7), 076401 (2016).
2. A. V. Kildishev, A. Boltasseva, and V. M. Shalae, “Planar photonics with metasurfaces,” *Science* **339**(6125), 1232009 (2013).
3. W. T. Chen, A. Y. Zhu, and F. Capasso, “Flat optics with dispersion-engineered metasurfaces,” *Nat. Rev. Mater.* **5**(8), 604–620 (2020).
4. V. A. Fedotov, M. Rose, S. L. Prosvirnin, *et al.*, “Sharp trapped-mode resonances in planar metamaterials with a broken structural symmetry,” *Phys. Rev. Lett.* **99**(14), 147401 (2007).
5. R. Singh, I. A. I. Al-Naib, M. Koch, *et al.*, “Sharp Fano resonances in THz metamaterials,” *Opt. Express* **19**(7), 6312–6319 (2011).
6. I. A. I. Al-Naib, C. Jansen, M. Koch, *et al.*, “High Q-factor metasurfaces based on miniaturized asymmetric single split resonators,” *Appl. Phys. Lett.* **94**(15), 153505 (2009).
7. Y. Wu, C. Li, X. Hu, *et al.*, “Applications of topological photonics in integrated photonic devices,” *Adv. Opt. Mater.* **5**, 1700357 (2017).
8. K. Koshelev and Y. Kivshar, “Dielectric Resonant Metaphotonics,” *ACS Photonics* **8**(1), 102–112 (2021).
9. S. Joseph, S. Pandey, S. Sarkar, *et al.*, “Bound states in the continuum in resonant nanostructures: an overview of engineered materials for tailored applications,” *Nanophotonics* **10**(17), 4175–4207 (2021).
10. X. Zhang, W. Shi, J. Gu, *et al.*, “Terahertz metasurface with multiple BICs/QBICs based on a split ring resonator,” *Opt. Express* **30**(16), 29088–29098 (2022).
11. L. L. Hale, T. Siday, and O. Mitrofanov, “Near-field imaging and spectroscopy of terahertz resonators and metasurfaces [Invited],” *Opt. Mater. Express* **13**(11), 3068 (2023).
12. G. R. Keiser and P. Klarskov, “Terahertz Field Confinement in Nonlinear Metamaterials and Near-Field Imaging,” *Photonics* **6**(1), 22 (2019).
13. C.-F. Wang, T. G. Habteyes, T. S. Luk, *et al.*, “Observation of Intersubband Polaritons in a Single Nanoantenna Using Nano-FTIR Spectroscopy,” *Nano Lett.* **19**(7), 4620–4626 (2019).
14. K. Monika Devi, S. Jana, and D. Roy Chowdhury, “Topological edge states in an all-dielectric terahertz photonic crystal,” *Opt. Mater. Express* **11**(8), 2445 (2021).
15. L. N. Casses, K. J. Kaltenecker, S. Xiao, *et al.*, “Quantitative near-field characterization of surface plasmon polaritons on monocrystalline gold platelets,” *Opt. Express* **30**(7), 11181–11191 (2022).
16. M. Schnell, A. García-Etxarri, A. J. Huber, *et al.*, “Controlling the near-field oscillations of loaded plasmonic nanoantennas,” *Nat. Photonics* **3**(5), 287–291 (2009).

17. R. Degl'Innocenti, R. Wallis, B. Wei, *et al.*, "Terahertz Nanoscopy of Plasmonic Resonances with a Quantum Cascade Laser," *ACS Photonics* **4**(9), 2150–2157 (2017).
18. S. Chen, A. Bylinkin, Z. Wang, *et al.*, "Real-space nanoimaging of THz polaritons in the topological insulator Bi₂Se₃," *Nat. Commun.* **13**(1), 1374 (2022).
19. M. Jeannin, G. Mariotti Nesurini, S. Suffit, *et al.*, "Ultrastrong Light–Matter Coupling in Deeply Subwavelength THz LC Resonators," *ACS Photonics* **6**(5), 1207–1215 (2019).
20. N. Sulollari, J. Keeley, S. Park, *et al.*, "Coherent terahertz microscopy of modal field distributions in micro-resonators," *APL Photonics* **6**(6), 066104 (2021).
21. O. Mitrofanov, I. Khromova, T. Siday, *et al.*, "Near-Field Spectroscopy and Imaging of Subwavelength Plasmonic Terahertz Resonators," *IEEE Trans. THz Sci. Technol.* **6**(3), 382–388 (2016).
22. I. Khromova, M. Navarro-Cfa, I. Brener, *et al.*, "Dipolar resonances in conductive carbon micro-fibers probed by near-field terahertz spectroscopy," *Appl. Phys. Lett.* **107**(2), 021102 (2015).
23. L. Thomas, T. Hannotte, C. N. Santos, *et al.*, "Imaging of THz Photonic Modes by Scattering Scanning Near-Field Optical Microscopy," *ACS Appl. Mater. Interfaces* **14**(28), 32608–32617 (2022).
24. O. Mitrofanov, Z. Han, F. Ding, *et al.*, "Detection of internal fields in double-metal terahertz resonators," *Appl. Phys. Lett.* **110**(6), 061109 (2017).
25. O. Mitrofanov, Y. Todorov, D. Gacemi, *et al.*, "Near-field spectroscopy and tuning of sub-surface modes in plasmonic terahertz resonators," *Opt. Express* **26**(6), 7437–7450 (2018).
26. M. M. Wiecha, S. Al-Daffaie, A. Bogdanov, *et al.*, "Direct Near-Field Observation of Surface Plasmon Polaritons on Silver Nanowires," *ACS Omega* **4**(26), 21962–21966 (2019).
27. A. Pizzuto, X. Chen, H. Hu, *et al.*, "Anomalous contrast in broadband THz near-field imaging of gold microstructures," *Opt. Express* **29**(10), 15190–15198 (2021).
28. L. L. Hale, Z. Wang, C. T. Harris, *et al.*, "Near-field spectroscopy of Dirac plasmons in Bi₂Se₃ ribbon arrays," *APL Photonics* **8**(5), 051304 (2023).
29. V. Pistore, L. Viti, C. Schiattarella, *et al.*, "Holographic Nano-Imaging of Terahertz Dirac Plasmon Polaritons in Topological Insulator Antenna Resonators," *Small* **20**(22), e2308116 (2024).
30. A. J. Huber, F. Keilmann, J. Wittborn, *et al.*, "Terahertz near-field nanoscopy of mobile carriers in single semiconductor nanodevices," *Nano Lett.* **8**(11), 3766–3770 (2008).
31. R. Mueckstein, C. Graham, C. C. Renaud, *et al.*, "Imaging and Analysis of THz Surface Plasmon Polariton Waves with the Integrated Sub-wavelength Aperture Probe," *J. Infrared, Millimeter, Terahertz Waves* **32**(8-9), 1031–1042 (2011).
32. P. Alonso-González, A. Y. Nikitin, Y. Gao, *et al.*, "Acoustic terahertz graphene plasmons revealed by photocurrent nanoscopy," *Nat. Nanotechnol.* **12**(1), 31–35 (2017).
33. E. A. A. Pogna, L. Viti, A. Politano, *et al.*, "Mapping propagation of collective modes in Bi₂Se₃ and Bi₂Te_{2.2}Se_{0.8} topological insulators by near-field terahertz nanoscopy," *Nat. Commun.* **12**(1), 6672 (2021).
34. A. Bhattacharya and J. Gómez Rivas, "Full vectorial mapping of the complex electric near-fields of THz resonators," *APL Photonics* **1**(8), 086103 (2016).
35. N. J. J. van Hoof, D. R. Abujetas, S. E. T. Ter Huurne, *et al.*, "Unveiling the symmetry protection of bound states in the continuum with terahertz near-field imaging," *ACS Photonics* **8**(10), 3010–3016 (2021).
36. H. Cai, J. Li, and L. Mao, "Experimental implementation for near-field displaying application of bound states in continuum supported by terahertz metasurfaces," *Opt. Express* **31**(2), 2654–2664 (2023).
37. T. Neuman, P. Alonso-González, A. Garcia-Etxarri, *et al.*, "Mapping the near fields of plasmonic nanoantennas by scattering-type scanning near-field optical microscopy," *Laser Photon. Rev.* **9**, 637–649 (2015).
38. G. Dai, Z. Yang, G. Geng, *et al.*, "Signal detection techniques for scattering-type scanning near-field optical microscopy," *Appl. Spectrosc. Rev.* **53**(10), 806–835 (2018).
39. C. Liu, P. Liu, C. Yang, *et al.*, "Terahertz metamaterial based on dual-band graphene ring resonator for modulating and sensing applications," *J. Opt.* **19**(11), 115102 (2017).
40. Y. Cheng, J. Yu, and X. Li, "Tri-band high-efficiency circular polarization convertor based on double-split-ring resonator structures," *Appl. Phys. B* **128**(1), 1 (2022).
41. J. García-García, F. Martín, J. D. Baena, *et al.*, "On the resonances and polarizabilities of split ring resonators," *J. Appl. Phys.* **98**(3), 033103 (2005).
42. C. Jansen, I. A. I. Al-Naib, N. Born, *et al.*, "Terahertz metasurfaces with high Q-factors," *Appl. Phys. Lett.* **98**(5), 051109 (2011).
43. Y. Lu, L. L. Hale, A. M. Zaman, *et al.*, "Near-Field Spectroscopy of Individual Asymmetric Split-Ring Terahertz Resonators," *ACS Photonics* **10**(8), 2832–2838 (2023).
44. O. Mitrofanov, M. Lee, J. W. P. Hsu, *et al.*, "Collection-mode near-field imaging with 0.5-THz pulses," *IEEE J. Select. Topics Quantum Electron.* **7**(4), 600–607 (2001).
45. H. A. Bethe, "Theory of Diffraction by Small Holes," *Phys. Rev.* **66**(7-8), 163–182 (1944).
46. L. L. Hale, J. Keller, T. Siday, *et al.*, "Noninvasive near-field spectroscopy of single subwavelength complementary resonators," *Laser Photon. Rev.* **14**, 1900254 (2020).
47. S. Kalthor, S. J. Kindness, R. Wallis, *et al.*, "Active Terahertz Modulator and Slow Light Metamaterial Devices with Hybrid Graphene-Superconductor Photonic Integrated Circuits," *Nanomaterials* **11**(11), 2999 (2021).